Supporting Information

Impact of Functional Groups on Cellulose Nanofibers on the State of Water Molecules, Photocatalytic Water Splitting, and Photothermal Water Evaporation

Weiming Zhou,[a, c] Hongqiang Huang,[a] Zequn Wang,[d] Swellam W. Sharshir,[a, e] Chong Wang,[a*] Meng An,[d*] Liwei Wang,[b*] and Zhanhui Yuan[a*]

a. College of Materials Engineering, Fujian Agriculture and Forestry University, Fuzhou 350002, China. Email: zhanhuiyuan@fafu.edu.cn and chongwang@fafu.edu.cn

b. College of Materials and Chemical Engineering, Minjiang University, Fuzhou 350108, China. Email: wlw@mju.edu.cn

c. College of Environmental and Resource Sciences, Fujian Normal University, Fuzhou 350117, China.

d. College of Mechanical and Electrical Engineering, Shaanxi University of Science and Technology, Xi'an 710021, China. Email: anmeng@sust.edu.cn

e. Mechanical Engineering Department, Faculty of Engineering, Kafrelsheikh University, Kafrelsheikh 33516, Egypt.

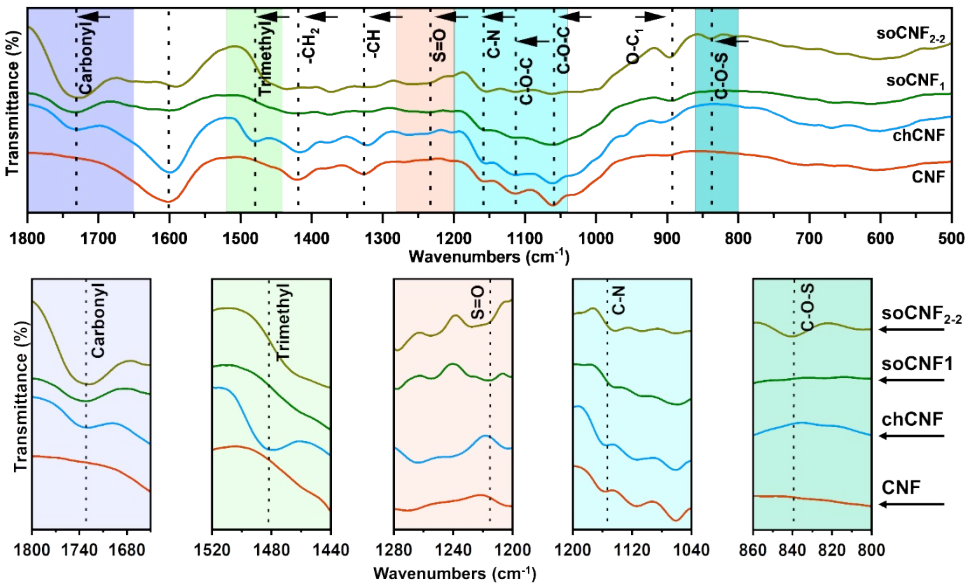

Fig. S1 FT-IR spectra of CNF, chCNF, soCNF$_1$ and soCNF$_{2\text{-}2}$.

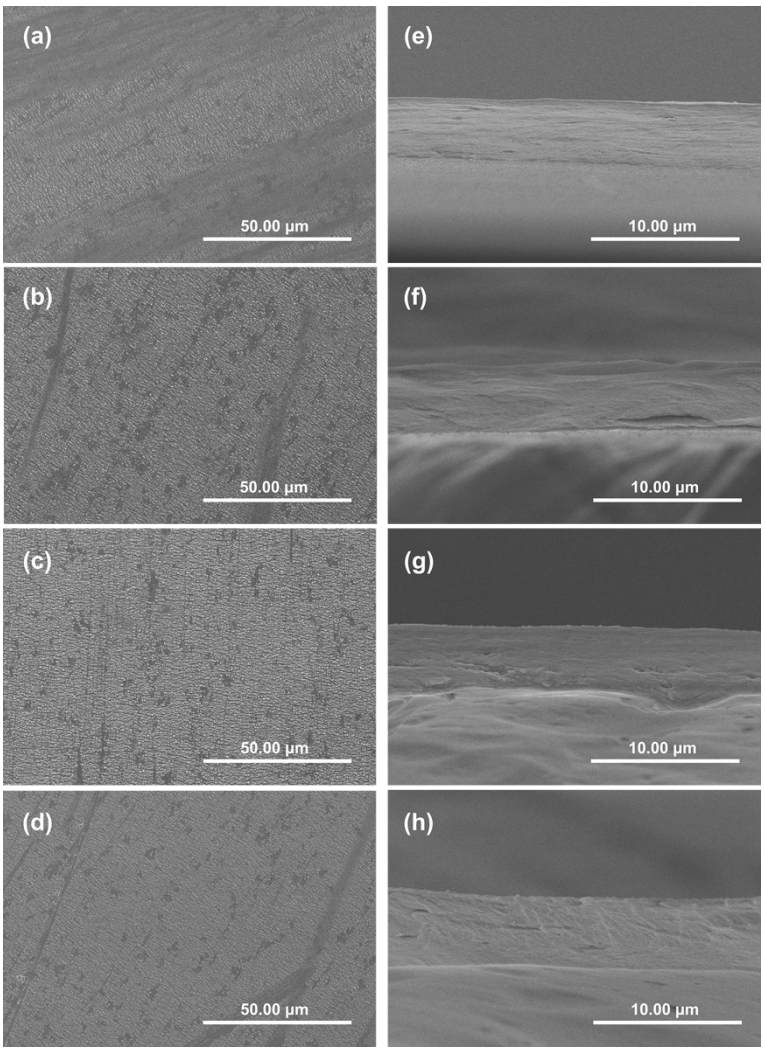

Fig. S2 Surface and cross-sectional SEM images of (a, e) CNFM, (b, f) chCNFM, (c, g) soCNF$_1$M and (d, h) soCNF$_{2\text{-}2}$M.

Fig. S2 depicts the surface and cross-sectional scanning electron microscopy (SEM) images of cellulose membranes. The results reveal that the surfaces of CNFM, chCNFM, soCNF$_1$M, and soCNF$_{2\text{-}2}$M exhibit a relatively flat morphology, and the presence of a directional arrangement of cellulose nanofibers (CNF) imparts a discernible orientation structure on their surfaces [1]. This is illustrated in **Fig. S2**e-h, which presents the cross-section images of the cellulose membrane. The thicknesses of CNFM, chCNFM, soCNF$_1$M, and soCNF$_{2\text{-}2}$M were calculated to be approximately 4.29, 4.56, 4.37, and 4.78 μm, respectively.

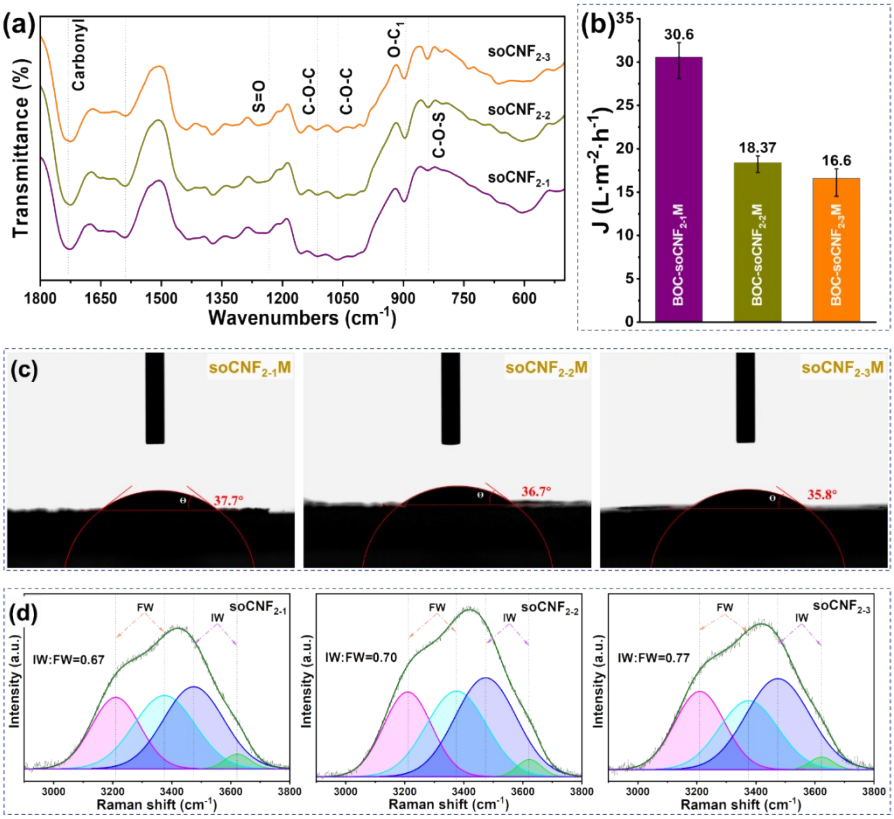

Fig. S3 (a) FT-IR spectra of soCNF$_{2\text{-}1}$, soCNF$_{2\text{-}2}$ and soCNF$_{2\text{-}3}$. (b) Water fluxes and (c) water contact angles of soCNF$_{2\text{-}1}$M, soCNF$_{2\text{-}2}$M and soCNF$_{2\text{-}3}$M. (d) Raman spectra and fitted curves of 1 wt.% soCNF$_{2\text{-}1}$, soCNF$_{2\text{-}2}$ and soCNF$_{2\text{-}3}$.

In Fig. **S3**a, the infrared spectra of different sulfonated celluloses reveal that the relative content of C-O-S groups in the prepared cellulose increases with the increasing dosage of chlorosulfonic acid. Fig. **S3**b illustrates the water flux of membranes prepared from sulfonated cellulose, with average water flux values for soCNF$_{2\text{-}1}$M, soCNF$_{2\text{-}2}$M, and soCNF$_{2\text{-}3}$M being 30.6, 18.37, and 16.6 L·m^{-2}·h^{-1}, respectively. As the sulfonic acid groups increase, hydrogen bonding between cellulose molecules strengthens,

resulting in denser cellulose membranes and, consequently, decreased water flux. The water contact angles of membranes with different sulfonic acid group contents are shown in Fig. **S3**c, and it is evident that water contact angles gradually decrease as the sulfonic acid groups in cellulose increase. Additionally, Raman spectroscopy was performed on 1 wt.% suspensions of $soCNF_2$ with different sulfonic acid group contents, and the calculated ratios of IW:FW for $soCNF_{2\text{-}1}$, $soCNF_{2\text{-}2}$, and $soCNF_{2\text{-}3}$ were 0.67, 0.70, and 0.77, respectively (Fig. **S3**d). This observation further confirms that the sulfonic acid group content affects the proportion of intermediate water.

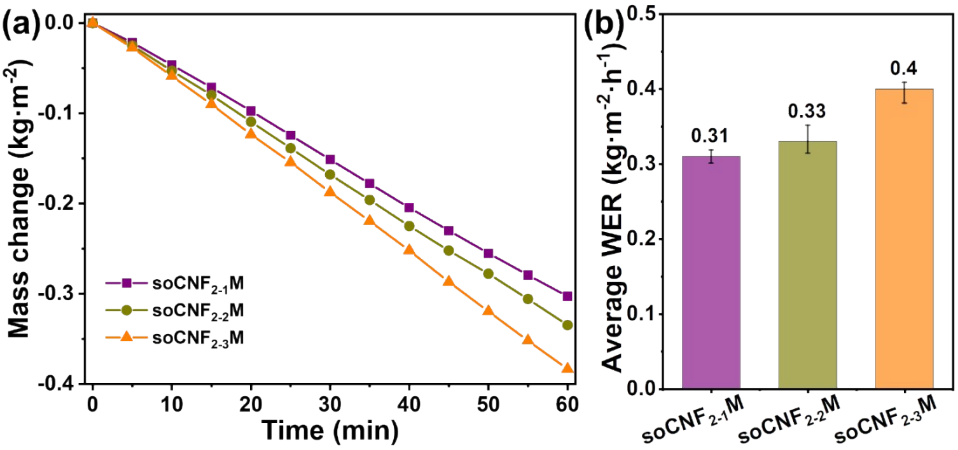

Fig. S4 (a) Mass change curves as a function of time and (b) evaporation rates of $soCNF_{2\text{-}1}M$, $soCNF_{2\text{-}2}M$ and $soCNF_{2\text{-}3}M$.

The above results demonstrate that different cellulose functional groups can lead to variations in water evaporation rates, and the content of these functional groups can also alter the proportion of intermediate water. Consequently, the water evaporation efficiency of cellulose with varying sulfonic acid group contents was tested, as shown in Fig. **S4**. As the sulfonic acid group content in cellulose increased, the water evaporation rate exhibited an increase from 0.31 $kg \cdot m^{-2} \cdot h^{-1}$ ($soCNF_{2\text{-}1}$) to 0.40 $kg \cdot m^{-2} \cdot h^{-1}$ ($soCNF_{2\text{-}3}$). The equivalent evaporation enthalpies for the prepared $soCNF_{2\text{-}1}M$, $soCNF_{2\text{-}2}M$, and $soCNF_{2\text{-}3}M$ were calculated using Equation 1 and found to be 800.5, 729.9, and 620.4 $J \cdot g^{-1}$, respectively.

Hence, it can be concluded that not only the type of functional groups in cellulose affects the state of water molecules, but also the content of these functional groups results in variations in the proportion of intermediate water, thereby causing differences

in water evaporation rates.

The enthalpy of evaporation reflects the actual energy required for water to change from the liquid phase to the gas phase in a solar evaporator, with lower evaporation enthalpy indicating less energy required. Under dark conditions, cellulose membranes with the same evaporative surface area (2×2 cm) were placed in a room at atmospheric pressure and 25°C with 45% humidity. It is assumed that under these conditions, both the evaporator and water evaporate at the same input power. The equivalent evaporation enthalpy can be estimated using the following formula [2]:

$$U_{in} = E_0 m_0 = E_{equ} m_g \quad (1)$$

In this equation, U_{in} represents the same input power during water evaporation (J), E_{equ} represents the equivalent evaporation enthalpy ($J \cdot g^{-1}$), E_0 represents the evaporation enthalpy of pure water (2256 $J \cdot g^{-1}$), m_0 represents the mass change of pure water, and m_g represents the mass change of the cellulose membrane evaporator.

After calculation, the equivalent evaporation enthalpies for the prepared CNFM, chCNFM, soCNF$_1$M, and soCNF$_{2\text{-}2}$M are 1034, 1551, 886.3, and 729.9 $J \cdot g^{-1}$, respectively. With modifications of functional groups on CNF, the soCNF$_{2\text{-}2}$M exhibits the lowest equivalent evaporation enthalpy, followed by soCNF$_1$M. This finding indicates that the hydrophilic sulfonic acid groups effectively reduce the energy required for water evaporation [3], a result consistent with the proportion of intermediate water obtained from Raman spectroscopy calculations. Furthermore, it validates that cellulose's hydrophilic functional groups can effectively improve the state of water molecules, leading to a reduction in its evaporation enthalpy.

The energy conversion efficiency (η) is calculated by the formula[4]:

$$\eta = m_e h_{LV} / C_{opt} P_0$$

Where m_e refers to the evaporation rate, h_{LV} is the enthalpy change of the evaporation enthalpy of water passing from its liquid to the gaseous phase, P_0 is the nominal solar illumination power of 1.0 Sun, and C_{opt} is the optical concentration on the evaporator surface. h_{LV} consists of the latent heat of evaporation and total enthalpy of sensible heat (315 $J \cdot g^{-1}$, from ca. 25 to 100 °C with specific heat capacity of water 4.18 $J \cdot g^{-1}$) [5, 6].

Table S1. Detailed parameters of photothermal water evaporation

Samples	pure water	BOC-CNFM	BOC-chCNFM	BOC-soCNF$_1$M	BOC-soCNF$_{2\text{-}2}$M
m_0 or m_g ($Kg{\cdot}m^{-2}{\cdot}h^{-1}$)	0.11	0.23	0.18	0.25	0.29
E_0 or E_{equ} ($J{\cdot}g^{-1}$)	2256	1078.96	1378.67	992.64	855.72
Surface temperature (^oC)	—	37.9	37.7	38.1	39
h_{LV} ($J{\cdot}g^{-1}$)	—	1132.88	1431.76	1047.4	914.24
m_e ($Kg{\cdot}m^{-2}{\cdot}h^{-1}$)	—	1.03	0.96	1.03	1.06
η (%)	—	0.2518	0.3102	0.2269	0.1955

The input heat flux is 1 kW·m^{-2}, and five main strategies for energy consumption are as follows: (1) water evaporation, (2) reflection energy loss, (3) conductive heat loss from the evaporator to the water, (4) radiation heat loss from the evaporator to the environment, and (5) convection heat loss from the evaporator to the environment[7]. The water evaporation consumption rate is equal to the evaporation conversion efficiency. Except for water evaporation, the remaining factors contribute to energy loss. It is noteworthy that a significant portion of the energy is not fully utilized, resulting in an energy loss ranging from 68.98% to 80.45%. In order to improve the efficiency of water evaporation, one effective approach is to incorporate high-efficiency photothermal conversion materials such as carbon-based materials [8].

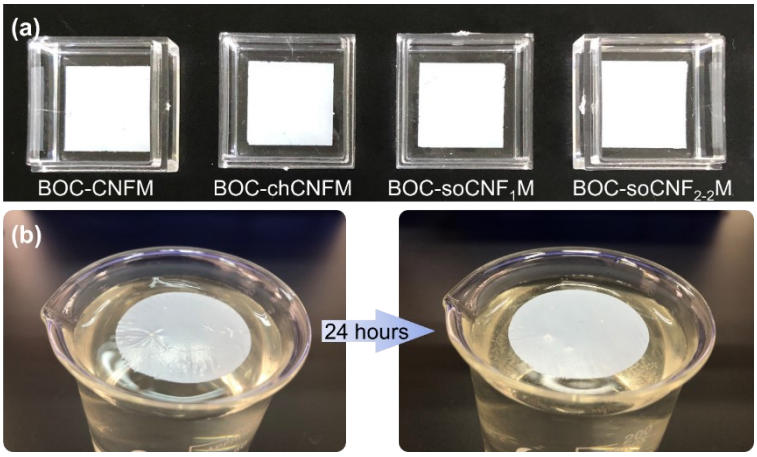

Fig. S5 (a) Stability in solution (float on water for 24 hours) of BOC-CNFM, BOC-chCNFM, BOC-soCNF$_1$M, and BOC-soCNF$_{2\text{-}2}$M. (b) The entire BOC-CNF$_{2\text{-}2}$M sample floats on the water.

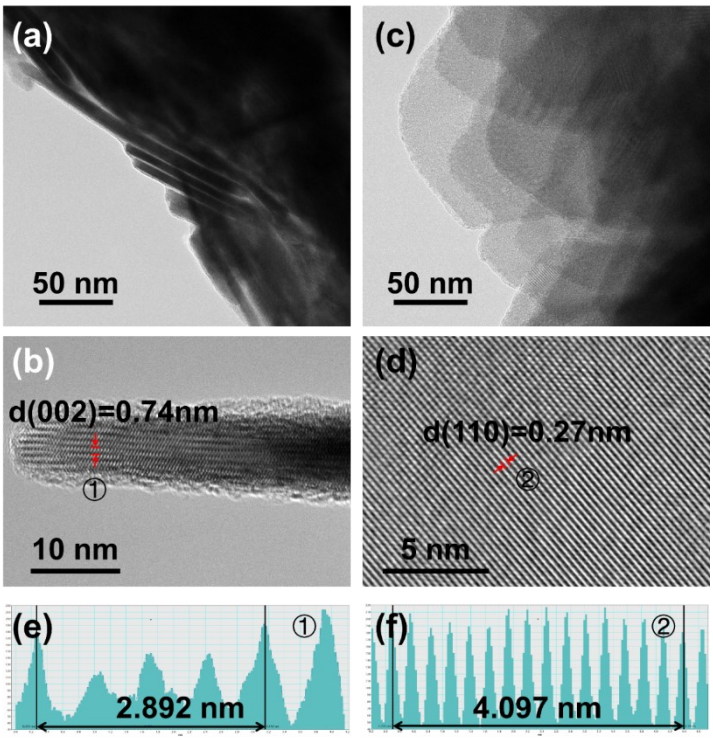

Fig. S6 (a, b) Side view and (c, d) top view and (h, j) HRTEM images of BNs, (e, f) intensity profiles in image (i) and (j), respectively.

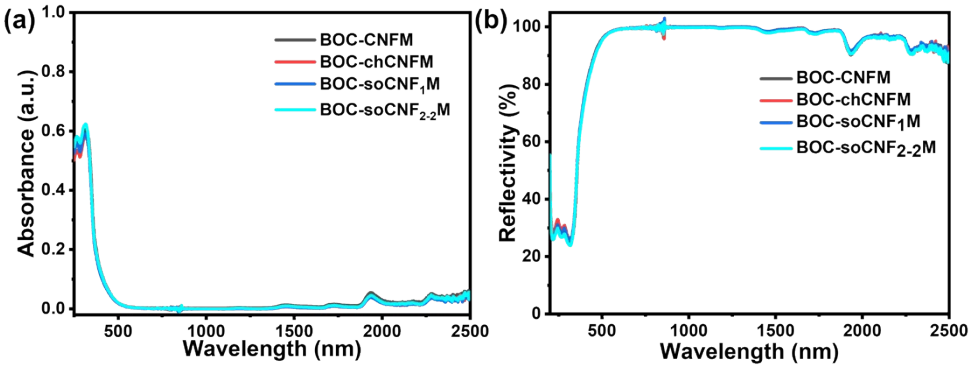

Fig. S7 (a) Absorption and (b) reflection curves of BOC-CNFM, BOC-chCNFM, BOC-soCNF$_1$M, and BOC-soCNF$_{2\text{-}2}$M.

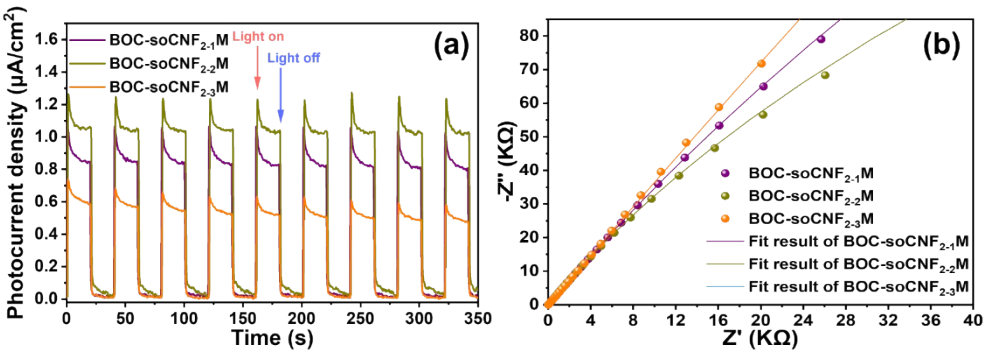

Fig. S8 (a) TPR curves and (b) EIS plots and fit results of BOC-soCNF$_{2\text{-}1}$M, BOC-soCNF$_{2\text{-}2}$M and BOC-soCNF$_{2\text{-}3}$M.

To further investigate the influence of sulfonic acid group content on the separation and transfer of photo-generated charge carriers, transient photocurrent response (TPR) and electrochemical impedance spectroscopy (EIS) were conducted on cellulose ($soCNF_2$) with varying sulfonic acid group contents when combined with BNs to create 2D lamellar membranes, as depicted in Fig. **S8**. As the sulfonic acid group quantity increased, the transient photocurrent density of the prepared 2D lamellar membranes followed the order: BOC-$soCNF_{2\text{-}2}$M > BOC-$soCNF_{2\text{-}1}$M > BOC-$soCNF_{2\text{-}3}$M (Fig. **S8**a). This suggests that the content of polar groups also affects the separation of photo-induced electrons and holes. Furthermore, an appropriate amount of sulfonic acid groups has a certain promoting effect on transient photocurrent, but when the quantity of sulfonic acid groups continues to increase, transient photocurrent decreases instead.

Additionally, as seen from the EIS plots in Fig. **S8**b, it can be observed that the impedance of 2D lamellar membranes prepared using cellulose ($soCNF_2$) with different sulfonic acid group contents follows this order: BOC-$soCNF_{2\text{-}3}$M > BOC-$soCNF_{2\text{-}1}$M > BOC-$soCNF_{2\text{-}2}$M. This indicates that there are variations in the interfacial charge transfer resistance associated with sulfonic acid group content, leading to changes in transient photocurrent density.

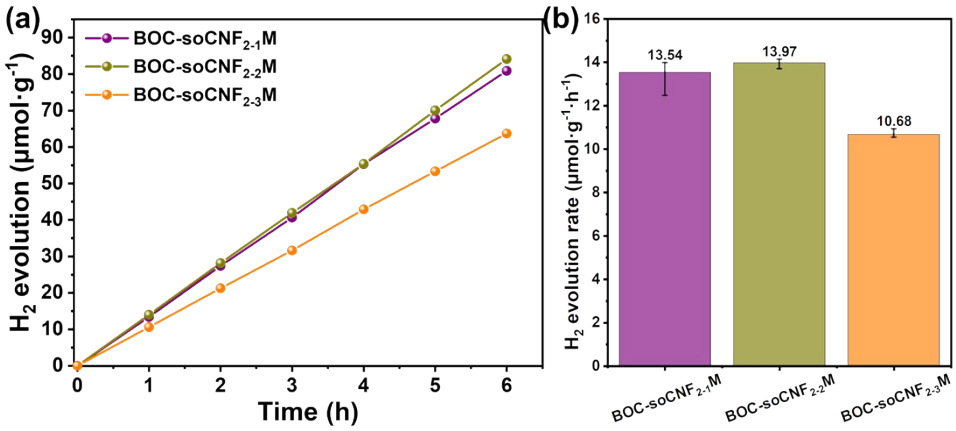

Fig. S9 PWS (a) activities and (b) rates of BOC-$soCNF_{2\text{-}1}$M, BOC-$soCNF_{2\text{-}2}$M and BOC-$soCNF_{2\text{-}3}$M.

Moreover, the hydrogen production performance of 2D lamellar membranes was also evaluated. As shown in Fig. **S9**, the hydrogen production rates of the lamellar membranes were as follows: 13.94 $\mu mol \cdot g^{-1} \cdot h^{-1}$ (BOC-$soCNF_{2\text{-}2}$M) > 13.54

μmol·g^{-1}·h^{-1} (BOC-soCNF$_{2\text{-}1}$M) > 10.68 μmol·g^{-1}·h^{-1} (BOC-soCNF$_{2\text{-}3}$M). Various factors influence PWS, primarily encompassing the four photocatalytic reaction processes of light absorption, charge separation, charge migration, and surface reaction, along with the reactivity of the reactant water. The introduction of sulfonic acid groups into CNF increases the content of intermediate water, consequently enhancing the reactivity of the reactant water. However, the polarity of the sulfonic acid groups in soCNF$_2$ also affects the ability of BN to separate photo-generated electrons and holes. Additionally, one-dimensional soCNF$_2$ can regulate the construction of the 2D lamellar membranes and the size of nanochannels through the interaction of functional groups with BN.

In summary, both the type and quantity of functional groups in CNF have an impact on the PWS performance of 2D lamellar membranes, primarily in terms of the construction of the 2D lamellar membranes and the reactivity of water. Moreover, appropriately polar functional groups and their quantity have a promoting effect on PWS.

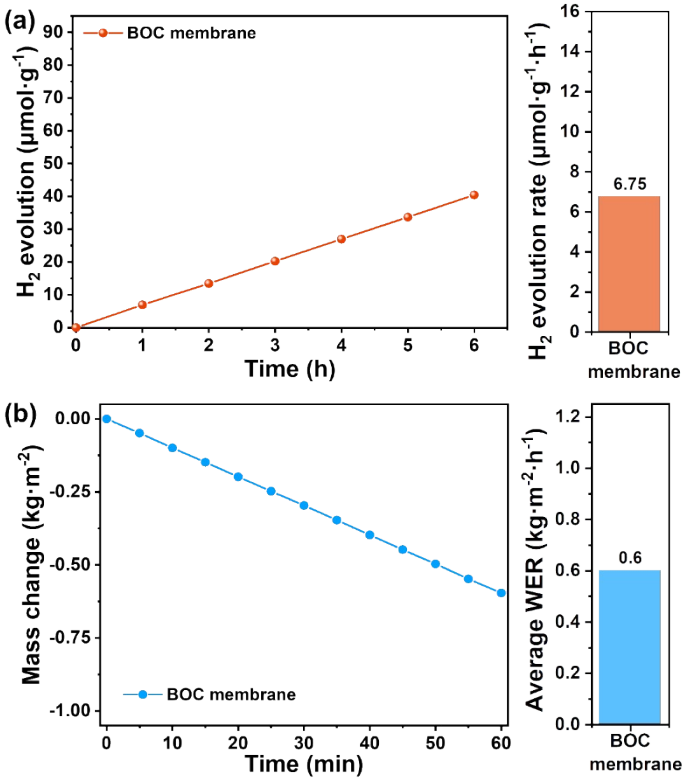

Fig. S10 (a) PWS activities and rates, (b) mass change curves as a function of time and evaporation rates of pure BOC lamellar membrane.

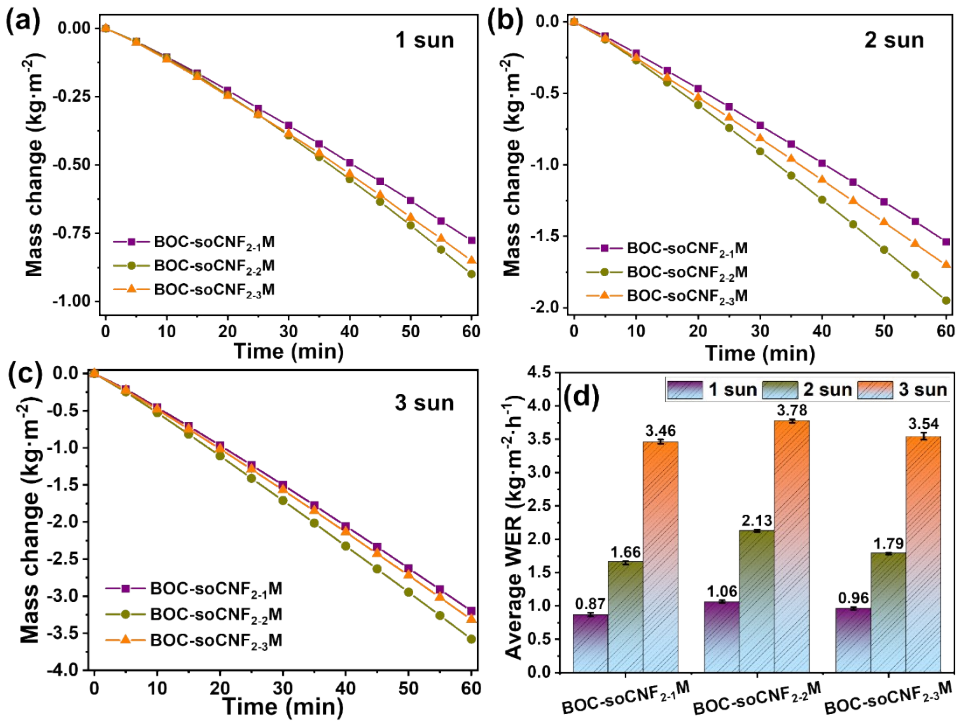

Fig. S11 (a-c) Mass change curves as a function of time and (d) evaporation rates of BOC-soCNF$_{2\text{-}1}$M, BOC-soCNF$_{2\text{-}2}$M and BOC-soCNF$_{2\text{-}3}$M under different power light intensities.

The PWE performance of 2D lamellar membranes, fabricated from cellulose (soCNF$_2$) with varying sulfonic acid group contents in combination with BN, is depicted in Fig. **S11**. As observed in the figure, the water evaporation rate initially increases with the rising sulfonic acid group content and subsequently decreases. Under 1.0 Sun illumination, the PWE rates were as follows: 1.06 kg·m^{-2}·h^{-1} (BOC-soCNF$_{2\text{-}2}$M) > 0.96 kg·m^{-2}·h^{-1} (BOC-soCNF$_{2\text{-}3}$M) > 0.87 kg·m^{-2}·h^{-1} (BOC-soCNF$_{2\text{-}1}$M) (Fig. **S11**a). Under 2.0 Sun illumination, the PWE rates were as follows: 2.13 kg·m^{-2}·h^{-1} (BOC-soCNF$_{2\text{-}2}$M) > 1.79 kg·m^{-2}·h^{-1} (BOC-soCNF$_{2\text{-}3}$M) > 1.66 kg·m^{-2}·h^{-1} (BOC-soCNF$_{2\text{-}1}$M) (Fig. **S11**b). Under 3.0 Sun illumination, the PWE rates were as follows: 3.78 kg·m^{-2}·h^{-1} (BOC-soCNF$_{2\text{-}2}$M) > 3.54 kg·m^{-2}·h^{-1} (BOC-soCNF$_{2\text{-}3}$M) > 3.46 kg·m^{-2}·h^{-1} (BOC-soCNF$_{2\text{-}1}$M) (Fig. **S11**c). Moreover, under 2.0 Sun illumination, the differences in the PWE rates among the three distinct sulfonic acid group content cellulose (soCNF$_2$) and BN-prepared 2D lamellar membranes were most pronounced. These results suggest that the content of cellulose functional groups also significantly influences the rate of PWE.

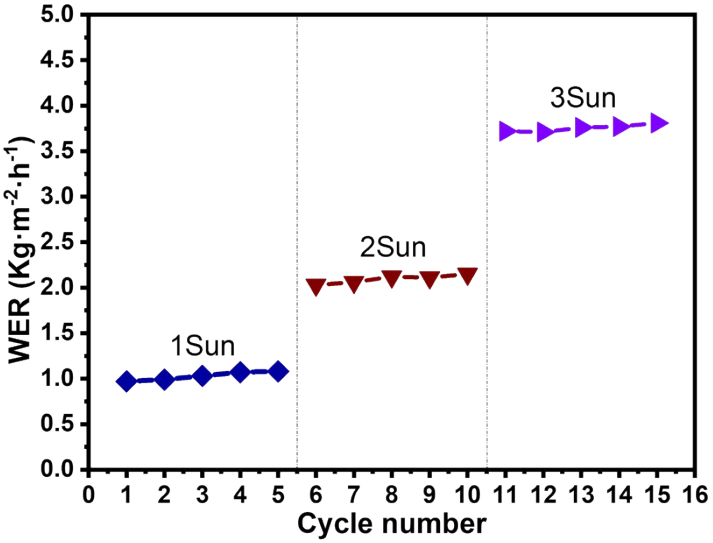

Fig. S12 Cycle performance of the BOC-soCNF$_{2\text{-}2}$M under different power light intensities.

In our previous study, we investigated the effect of 2D lamellar membranes with different BN loads on PWS and PWE performance [9, 10]. As the thickness of 2D lamellar membranes increases, the water transfer length rises, and the water flux decreases (**Fig. S13a**). Notably, there is a significant decrease in light intensity in the vertical direction of the lamellar membrane (**Fig. S13b**). This reduction in light intensity with the lamellar membrane's vertical direction is a crucial factor influencing photocatalytic activity. Consequently, a lamellar membrane that is too thick will make photocatalytic reactions at the bottom impossible, increase the length of mass transport channels, and hinder mass transfer efficiency. Therefore, maintaining an optimal thickness of the lamellar membranes is crucial for ensuring complete light absorption and optimizing photocatalytic efficiency (**Fig. S13c-e**).

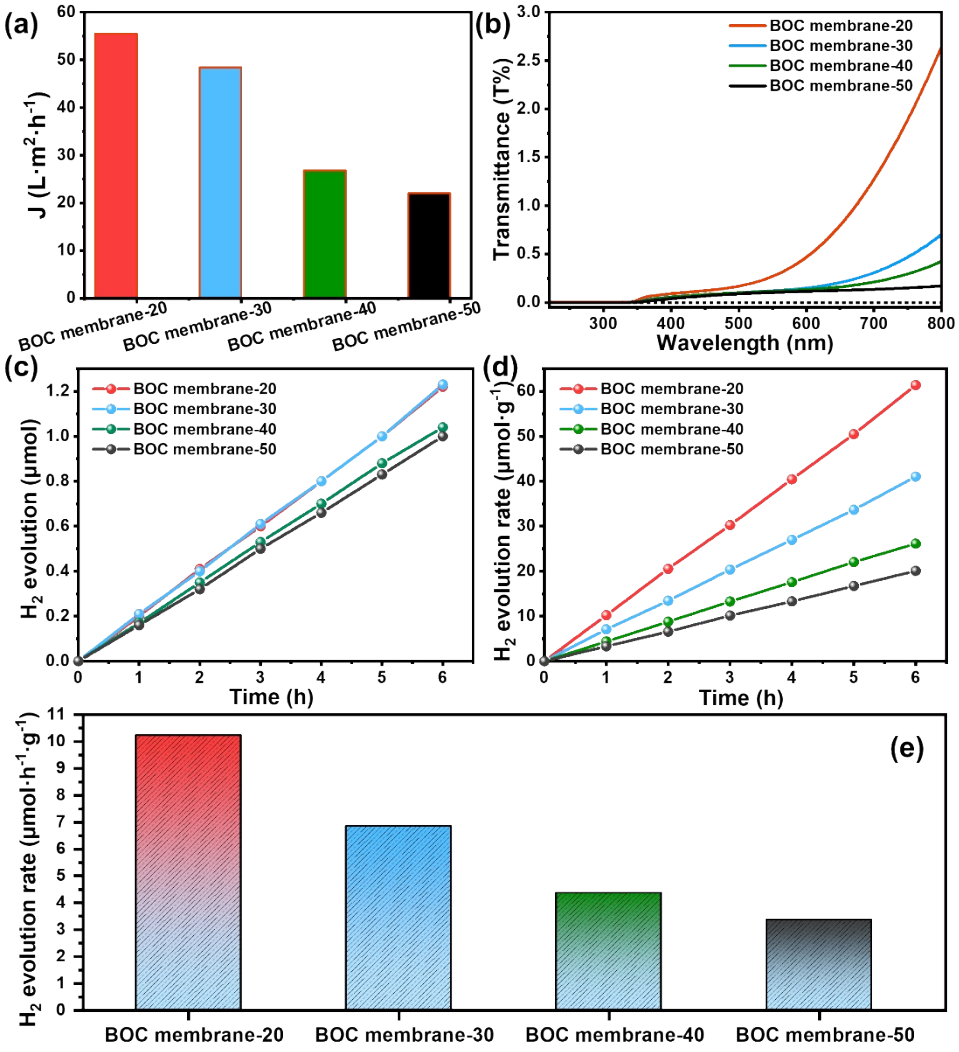

Fig. S13. (a) Water flux, (b) UV-vis transmission spectra, and (c-e) PHE of different thickness BOC membranes. The thickness of lamellar membranes was accurately controlled by the loading capacity of BNs, BOC membrane-20, BOC membrane-30, BOC membrane-40 and BOC membrane-50 correspond to 20, 30, 40 and 50 mg BNs per membrane with same diameter (3.8 cm).

Similarly, as outlined in our previous study[10], the thickness of 2D lamellar membranes prepared with BNs and CNF@CNT (BOC-CNF@CNTM) was controlled by the mass of the BNs, and the PWE performance was tested. By increasing the mass of BNs from 20 to 50 mg, the free-standing 2D lamellar membranes could be separated from the porous substrate (**Fig. S14a**). Additionally, IR images show that the surface temperature of 2D lamellar membranes with different thicknesses does not change significantly (**Fig. S14b**). As the thickness increases, the path of water transport becomes longer. However, the thickness of the 2D lamellar membranes is relatively thin. Among these, the thickness of the BOC-CNF@CNTM with 30 mg BNs is 4.53

μm, ensuring the required water supply for PWE and resulting in a small impact with a slight decrease in the PWE rate (**Fig. S14c, d**).

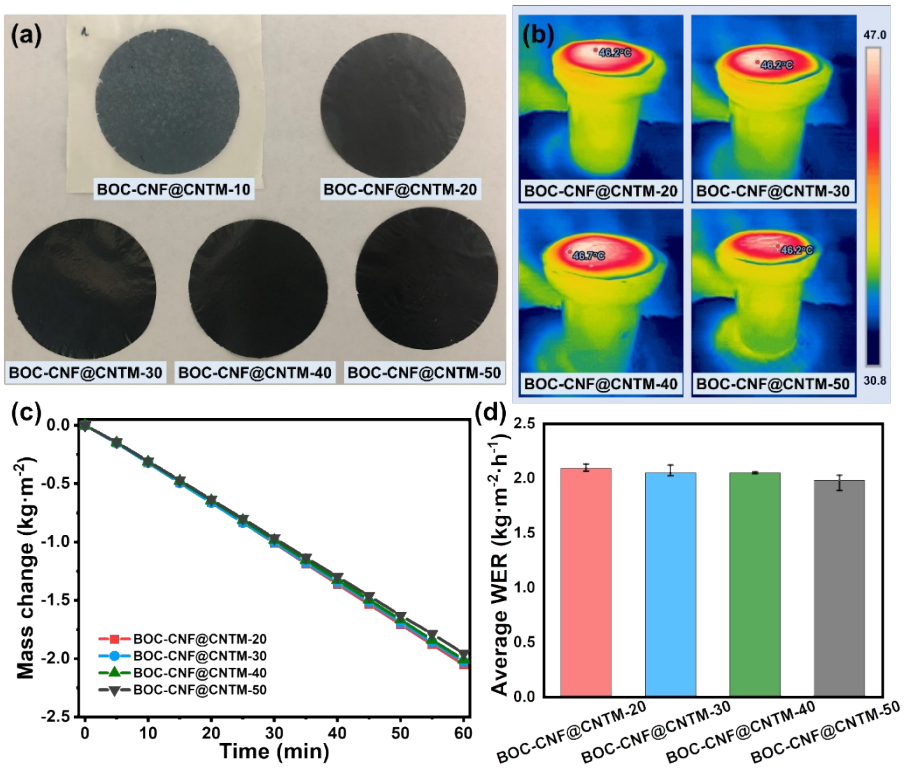

Fig. S14 (a) Optical photograph, (b) IR images of as-prepared samples under 1 sun irradiation, (c) mass change curves as a function of time, and (d) evaporation rates of BOC-CNF@CNTM with different thickness. The thickness of lamellar membranes is accurately controlled by the loading capacity of BNs, BOC-CNF@CNTM-10, BOC-CNF@CNTM-20, BOC-CNF@CNTM-30, BOC-CNF@CNTM-40 and BOC-CNF@CNTM-50 correspond to 10, 20, 30, 40 and 50 mg BNs per membrane with same diameter (3.8 cm). BOC-CNF@CNTM-10 is less likely to be separated from the porous substrate into a free-standing membranes.

The nitrogen adsorption-desorption isotherm of BOC-CNFM was measured to analyze the type and size of the nanochannels in the membrane. As illustrated in **Fig. S15a**, the BOC-CNFM exhibited a hysteresis loop typical of slit-like pores formed during the membrane fabrication process. The Brunauer-Emmett-Teller specific surface area of BOC-CNFM was measured and found to be 1.742 $m^2 \cdot g^{-1}$ (**Fig. S15a**). The pore size distribution diagram calculated by the BJH method in **Fig. S15b** showed that many mesoporous were present in the samples [11].

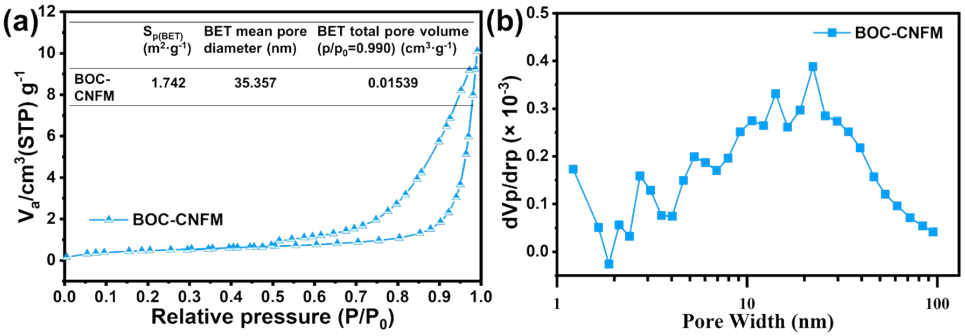

Fig. S15 (a) N_2 adsorption/desorption isotherm and (b) pore size distribution of BOC-CNFM.

The measured thickness of the BOC-CNFM, BOC-chCNFM, BOC-soCNF$_1$M and BOC-soCNF$_{2\text{-}2}$M membranes is approximately 4.80, 5.30, 4.75 and 4.73 μm, respectively (**Fig. 8a-d**). Notably, the thickness of the composite lamellar membranes is relatively consistent, indirectly indicating that the internal empty structure has not changed significantly.

Table S2. PWS activities of representative BiOCl-based photocatalysts.

Photocatalyst	Hole scavenger	Light Source	Hydrogen production rate ($\mu mol \cdot h^{-1} \cdot g^{-1}$)	Reference
BiOCl	Na_2S and Na_2SO_3	300 W Xenon lamp, full spectrum	2.22	12
Bulk BiOCl	TEOA	300 W Xenon lamp, $\lambda > 420$ nm	2.4	13
Black ultrathin BiOCl			50.2	
BiOCl	Methanol	500 W Xenon lamp, full spectrum	~5	14
Ultrathin BiOCl	Na_2SO_4	300 W Xenon lamp, $\lambda > 420$ nm	62.4	15
Ultrathin BiOCl	No	500 W Xenon lamp, full spectrum	35	16
BiOCl nanosheet	TEOA	300 W Xenon lamp, full spectrum	2.66	9
BiOCl 2D lamellar membrane			6.75	
BiOCl/CNFs 2D lamellar membrane	TEOA	300 W Xenon lamp, full spectrum	12.49	11
BiOCl@Pt 3%	Methanol	500 W Xenon lamp, full spectrum	~7.5	14
BiOCl/copper(II) phthalocyanine			~20	
$Bi_6O_6(OH)_3(NO_3)_3 \cdot 1.5H_2O$–BiOCl	TEOA	300 W Xenon lamp, full spectrum	6.27	17
BiOCl/Au/MnO_x	No	500 W Xenon lamp, full spectrum	10.7	18
BiOCl(110)-PbS	Na_2S and Na_2SO_3	300 W Xenon lamp, full spectrum	16	12
Fe(III) modified BiOCl ultrathin nanosheet	Na_2SO_4	300 W Xenon lamp, $\lambda > 420$ nm	141.6	15
Carbon-doped BiOCl/NiO_x	TEOA	300 W Xenon lamp, full spectrum	420	19
4% BiOCl@$ZnIn_2S_4$/ 0.0625 wt% Pt	Glycerol	1000 W Xenon lamp, λ>420 nm	674	20
BiOX/$CuFe_2O_4$	Methanol	250 W Xe lamp, visible light	740	21
Eosin Y-sensitized Sn-doped ZnO/BiOCl	TEOA	300 W Xenon lamp, full spectrum	4146.77	22
BiOCl/β-FeOOH	TEOA	500 W Xenon lamp, full spectrum	16640	23
MoS_2/$Bi_{12}O_{17}Cl_2$ bilayer	Ascorbic acid	300 W Xenon lamp, $\lambda > 420$ nm	33000	24

Table S3. Water evaporation performance of previously reported semiconductor solar thermal evaporators.

Materials	Evaporation rate ($kg \cdot m^{-2} \cdot h^{-1}$)	References
Metal oxides		
Ti^{3+}-TiO_2	1.2	25
Quasi-metallic $WO_{2.9}$ nanorods	1.28	26
Black TiO_2 film	1.3	27
Ni-NiO_x/Ni foam	1.41	28
N-doped $WO_{2.9}$	1.45	29
Metal chalcogenides		
CuS nanoflower	1.09	30
Cu_xS film	1.12	31
Hollow CuS nanocubes	1.34	32
2D/2D Ti_3C_2/MoS_2 nanocomposites	1.36	33
1D/2D TiO_2@MoS_2	1.42	34
TiO_2 NWAs@MoS_2/Ti mesh	1.42	34
Bismuth oxychloride		
Surface defect-modified Bi/BiOCl	1.25	35
Bi/BiOCl	1.47	36
MoO_{3-x}-BiOCl-CNTs	7.75*	37
Other types of semiconductor		
LaB_6/melamine sponge	1.13	38
molybdenum carbide based polyvinyl alcohol hydrogels (MoC_xPH)	1.59	39
CuS/bacterial cellulose	1.44	40
TiO_2@TiN/carbonized wood	1.47	41
Hydrogenated TiO_{2-x}/Cs_xWO_3/Ti mesh	1.46	42
Oxygen vacancy defect-HNb_3O_8	1.4	43
Multifunctional CuO nanowire mesh	1.42	44
Semiconductor and carbon-based material		
TiN/bio-carbon foam	1.26	41
$BiVO_4$-rGO	1.6	45
Co_3O_4@PDA-rGO photothermal aerogel	1.60 (2D) 3.71 (3D)	46
rGO/FeOOH	1.94	47
FeO_x-rGO	2.04	48

* Note: Solar light-driving evaporation was tested using a solar simulator (300 W)

References

1. M. Giese and M. Spengler, *Mol. Syst. Des. Eng.*, 2019, **4**, 29-48.
2. K. Sheng, M. Tian, J. Zhu, Y. Zhang and B. Van der Bruggen, *ACS Nano*, 2023, **17**, 15482-15491.
3. J. Ren, L. Chen, J. Gong, J. Qu and R. Niu, *Chem. Eng. J.*, 2023, **458**, 141511.
4. S. Yan, H. Song, Y. Li, J. Yang, X. Jia, S. Wang and X. Yang, *Appl. Catal., B*, 2022, **301**, 120820.
5. Z. Wei, C. Cai, Y. Huang, Y. Wang and Y. Fu, *Nano Energy*, 2021, **86**, 106138.
6. B. Wen, X. Zhang, Y. Yan, Y. Huang, S. Lin, Y. Zhu, Z. Wang, B. Zhou, S. Yang and J. Liu, *Desalination*, 2021, **516**, 115228.
7. N. Xu, X. Hu, W. Xu, X. Li, L. Zhou, S. Zhu and J. Zhu, *Adv Mater*, 2017, **29**, 1606762.
8. Y. Li, Y. Shi, H. Wang, T. Liu, X. Zheng, S. Gao and J. Lu, *Carbon Energy*, 2023, **5**, e331.
9. W. Zhou, Y. Wu, H. Huang, M. Zhang, X. Sun, Z. Wang, F. Zhao, H. zhang, T. Xie, M. An, L. Wang and Z. Yuan, *Renew. Sust. Energ. Rev.*, 2022, **168**, 112767.
10. W. Zhou, H. Huang, Y. Wu, J. Wang, Y. Yamauchi, J. Kim, S. M. Osman, X. Xu, L. Wang, C. Wang and Z. Yuan, *Chem. Eng. J.*, 2023, **471**, 144395.
11. W. Zhou, Z. Wang, H. Huang, Y. Wu, A. A. Alothman, M. Ouladsmane, Y. Yamauchi, X. Xu, M. An, L. Wang and Z. Yuan, *Chem. Eng. J.*, 2023, **456**, 140933.
12. J. Lu, Y. Chen, L. Li, X. Cai, S. Zhong, L. Wu, J. Chen and S. Bai, *Chem. Eng. J.*, 2019, **362**, 1-11.
13. L. Ye, X. Jin, Y. Leng, Y. Su, H. Xie and C. Liu, *J. Power Sources*, 2015, **293**, 409-415.
14. L. Zhang, W. Wang, S. Sun, Y. Sun, E. Gao and J. Xu, *Appl. Catal., B*, 2013, **132-133**, 315-320.
15. Y. Mi, L. Wen, Z. Wang, D. Cao, R. Xu, Y. Fang, Y. Zhou and Y. Lei, *Nano Energy*, 2016, **30**, 109-117.
16. L. Zhang, Z. Han, W. Wang, X. Li, Y. Su, D. Jiang, X. Lei and S. Sun, *Chemistry*, 2015, **21**, 18089-18094.
17. S. Sun, Y. Jiang, W. Xiao, W. Zhou, L. Wang and Z. Yuan, *Front. Mater. Sci.*, 2021, **15**, 299-304.
18. L. Zhang, W. Wang, S. Sun, D. Jiang and E. Gao, *Appl. Catal., B*, 2015, **162**, 470-474.
19. J. Li, K. Zhao, Y. Yu and L. Zhang, *Adv. Funct. Mater.*, 2015, **25**, 2189-2201.
20. O. Cavdar, M. Baluk, A. Malankowska, A. Zak, W. Lisowski, T. Klimczuk and A. Zaleska-Medynska, *J. Colloid Interface Sci.*, 2023.
21. S. Bera, S. Ghosh, T. Maiyalagan and R. N. Basu, *ACS Appl. Energy Mater.*, 2022, **5**, 3821-3833.
22. Y. Guo, C. Qi, B. Lu and P. Li, *Int. J. Hydrogen Energy*, 2022, **47**, 228-241.
23. W. Li, S.-a. He, X. Wang, Q. Ma and C.-h. Zhao, *Int. J. Energy Res.*, 2019, **43**, 2162-2171.
24. J. Li, G. Zhan, Y. Yu and L. Zhang, *Nat. Commun.*, 2016, **7**, 11480.
25. P. Ying, M. Li, F. Yu, Y. Geng, L. Zhang, J. He, Y. Zheng and R. Chen, *ACS Appl Mater Interfaces*, 2020, **12**, 32880-32887.
26. L. Sun, Z. Li, R. Su, Y. Wang, Z. Li, B. Du, Y. Sun, P. Guan, F. Besenbacher and M. Yu, *Angew. Chem. Int. Ed.*, 2018, **57**, 10666-10671.
27. I. Zada, W. Zhang, P. Sun, M. Imtiaz, N. Iqbal, U. Ghani, R. Naz, Y. Zhang, Y. Li, J. Gu, Q. Liu, D. Pantelić, B. Jelenković and D. Zhang, *Appl. Mater. Today*, 2020, **20**, 100669.
28. D. Wu, D. Qu, W. Jiang, G. Chen, L. An, C. Zhuang and Z. Sun, *J. Mater. Chem. A*, 2019, **7**,

8485-8490.
29. H. Yang, Y. Liu, Z. Qiao, X. Li, Y. Wang, H. Bao, G. Yang and X. Li, *Appl. Surf. Sci.*, 2021, **555**, 149697.
30. F. Tao, Y. Zhang, S. Cao, K. Yin, X. Chang, Y. Lei, R. Fan, L. Dong, Y. Yin and X. Chen, *Mater. Today Energy*, 2018, **9**, 285-294.
31. Z. Guo, X. Ming, G. Wang, B. Hou, X. Liu, T. Mei, J. Li, J. Wang and X. Wang, *Semicond. Sci. Technol.*, 2018, **33**, 025008.
32. L. Su, Y. Hu, Z. Ma, L. Miao, J. Zhou, Y. Ning, Z. Chang, B. Wu, M. Cao, R. Xia and J. Qian, *Sol. Energy Mater. Sol. Cells*, 2020, **210**, 110484.
33. R. Xu, N. Wei, Z. Li, X. Song, Q. Li, K. Sun, E. Yang, L. Gong, Y. Sui, J. Tian, X. Wang, M. Zhao and H. Cui, *J. Colloid Interface Sci*, 2021, **584**, 125-133.
34. B. Yuan, L. Meng, C. Zhang, L. Yang, L. Bai, H. Yang, D. Wei, F. Wang, Q. Wang, W. Wang and H. Chen, *Appl. Surf. Sci.*, 2021, **570**, 151143.
35. H. Yang, G. Yang, Z. Qiao, Y. Yang, S. Zhang, X. Li and Y. Liu, *J. Alloys Compd.*, 2020, **836**, 155380.
36. X. Li, Y. Pang, Y. Zhang, B. Ge, J. Liu, Y. Zhang, L. Zhao, G. Ren and Z. Zhang, *Sep. Purif. Technol.*, 2023, **326**, 124804.
37. Z. Gao, H. Yang, J. Li, L. Kang, L. Wang, J. Wu and S. Guo, *Appl. Catal., B*, 2020, **267**, 118695.
38. C. Zhang, B. Yuan, L. Yang, L. Bai, H. Yang, D. Wei, W. Wang, Y. Liang, Q. Wang and H. Chen, *J. Am. Ceram. Soc.*, 2020, **103**, 3466-3472.
39. F. Yu, X. Ming, Y. Xu, Z. Chen, D. Meng, H. Cheng, Z. Shi, P. Shen and X. Wang, *Adv. Mater. Interfaces*, 2019, **6**, 1901168.
40. D. Zhang, M. Zhang, S. Chen, Q. Liang, N. Sheng, Z. Han, Y. Cai and H. Wang, *Desalination*, 2021, **500**, 114899.
41. D. Guo and X. Yang, *Sci. China Mater.*, 2018, **62**, 711-718.
42. B. Yuan, C. Zhang, Y. Liang, L. Yang, H. Yang, L. Bai, D. Wei, W. Wang, Q. Wang and H. Chen, *Sol. RRL*, 2021, **5**, 2100105.
43. M. Q. Yang, C. F. Tan, W. Lu, K. Zeng and G. W. Ho, *Adv. Funct. Mater.*, 2020, **30**, 2004460.
44. Y. Xu, J. Ma, Y. Han, J. Zhang, F. Cui, Y. Zhao, X. Li and W. Wang, *ACS Sustainable Chem. Eng.*, 2019, **7**, 5476-5485.
45. L. Noureen, Z. Xie, M. Hussain, M. Li, Q. Lyu, K. Wang, L. Zhang and J. Zhu, *Sol. Energy Mater. Sol. Cells*, 2021, **222**, 110952.
46. T. Gao, X. Wu, G. Owens and H.-L. Xu, *Tungsten*, 2020, **2**, 423-432.
47. J. Ma, Z. Guo, X. Han, K. Guo, H. Li, P. Fang, X. Wang and J. Xin, *Carbon*, 2023, **201**, 318-327.
48. Y. Sun, X. Zhao, X. Song, J. Fan, J. Yang, Y. Miao and S. Xiao, *J. Environ. Sci.*, 2024, **138**, 671-683.